J. Feng, X. Hou, P. Di Lizia, R. Armellin, D.A. Santeramo
Sensitivity Analysis of the Orbital Motion Around 469219 Kamo'oalewa (2016 HO3) to Uncertainties on Asteroid Mass and Solar Radiation Pressure
Advances in Space Research, Vol. 69, N. 3, 2022, p. 1602-1618
doi:10.1016/j.asr.2021.11.035

Sensitivity analysis of the orbital motion around 469219 Kamo'oalewa (2016 HO_3) to uncertainties on asteroid mass and solar radiation pressure

Jinglang Feng[1], Xiyun Hou[2], Pierluigi Di Lizia[3], Roberto Armellin[4], Daniele Antonio Santeramo[3]

1 University of Strathclyde, United Kingdom, fjlangabc@gmail.com
2 Nanjing University, China, silence@nju.edu.cn
3 Politecnico di Milano, Italy, pierluigi.dilizia@polimi.it, danieleantonio.santeramo@polimi.it
4 The University of Auckland, New Zealand, roberto.armellin@auckland.ac.nz

Abstract
This study investigates the robustness of orbital motion in the vicinity of the asteroid 469219 Kamo'oalewa (2016 HO_3) considering the uncertainties of its mass and the solar radiation pressure. By applying the automatic domain splitting algorithm, these uncertainties are propagated and their effects on orbits with different geometries are investigated. Moreover, the bounds of the state flow are also evaluated along the propagation as an indicator of the motion sensitivity to uncertainties. An analysis of the results obtained shows that polar orbits are more robust to these uncertainties than equatorial and inclined orbits. Specifically, the solar terminator orbit is bounded within a small range and has the best robustness among all the polar orbits, thus can be used for practical mission purposes. Our studies prove that robust orbits exist even for very small bodies with weak gravity fields. Therefore, this work contributes to systematically identifying robust motions near an asteroid when uncertainties of the gravity and the SRP are simultaneously considered, addressing the challenge of real mission operations.
Keywords: 469219 Kamo'oalewa (2016 HO_3), gravity uncertainty, automatic domain splitting, uncertainty propagation, robustness, solar radiation pressure

1 Introduction

Small solar system bodies have become the popular targets of deep space missions, due to their scientific and technical advantages as near-Earth valuable natural resources. The recent and future missions include JAXA's Hayabusha2 to the asteroid Ryugu (Watanabe et al., 2017), NASA's OSIRIS-Rex to Bennu (Lauretta et al., 2017), NASA's DART mission (Cheng et al., 2018) and ESA's HERA mission (Pellacani et al., 2019) both to the binary asteroid Dydimos, and NASA's Janus mission (Scheeres et al., 2020) to two binary asteroid systems 1996 FG3 and 1991 VH. China is also planning its first asteroid mission and 2016 HO_3 is a target (Zhang et al., 2019). 2016 HO_3 is currently the smallest and closest quasi-satellite of Earth (de la Fuente Marcos & de la Fuente Marcos, 2016) with an estimated diameter of about 40 m and, as a consequence, a very weak surface gravity. The recent updated studies about its orbital evolution and physical properties can be found in Dora et al. (2018) and Gur'yanov and Galushina (2021). However, due to its small size and the limited amount of ground-based optical and radar observations, its shape and mass have been estimated with large uncertainties before the spacecraft's arrival, which brings about uncertainty to mission orbit design and prediction. As a result of the weak gravity of 2016 HO_3, the solar radiation pressure (SRP) is an important perturbation on the orbital motion around 2016 HO_3 and it should be considered in the dynamics. Moreover, the SRP usually cannot be accurately modeled due to non-complete understanding of the reflection properties of all the surfaces of the spacecraft. Therefore, considering these uncertainties, identifying the robust region of motion in the vicinity of asteroid 2016 HO_3 is paramount to the preliminary design of a mission.

There are various methods of propagating uncertainty, including the linearized ones and the non-linear ones, respectively. The former type generally applies the state transition matrix (STM) to map the deviation of the initial state of a trajectory to that of the final state. The eigenvalues of the STM

indicate the linear stability of this trajectory (Arnold, 1989). The latter type includes many different methods that address the deficiencies of the linearization. The Monte Carlo (MC) method is a commonly used one by performing point-wise numerical simulations of the fully nonlinear dynamics, providing statistics of the true trajectory. However, it is computationally intensive and the time consumption increases with the increasing number of samples (Maybeck, 1982). By approximating the arbitrary initial distribution with a limited number of samples, with a finite sum of weighted Gaussian distributions and with polynomial series, respectively, the unscented transformation (UT, Julier et al., 1995), the Gaussian mixtures model (GMM, Terejanu et al., 2008) and the polynomial chaos expansion (PCE, Wiener, 1938) have been developed. They are classified as non-intrusive methods since they do not require access to the dynamical equations and treat them as a black box. Their main drawbacks are that the number of samples (e.g. UT) and the number of expansion terms (e.g. PCE) change linearly and exponentially with the dimension of input uncertainties respectively, which is computationally expensive for large-dimensional uncertainties of complex systems.

An alternative way to deal with the nonlinearity is based on approximating the flow of the dynamics with Taylor or polynomial series. This method requires the dynamical equations of the system and is categorized as an intrusive method. In particular, the general polynomial algebra (GPA) was recently developed to approximate the flow of the dynamics in multivariate and generic polynomial expansions (Vasile et al., 2019). It performs well in propagating uncertainty sets through nonlinear dynamical systems. The differential algebra (DA) method relies on the computation of Taylor expansion of the flow of the dynamics up to arbitrary order with automatic differentiation (Berz, 1999). The final output of DA is a list of final state polynomials, each describing the evolution of the initial conditions i.e. mapping the entire initial domain into the final set. Moreover, instead of running thousands of point-wise integrations of the Monte Carlo method, the integrations of DA are performed by the fast evaluation of the Taylor polynomials that are just algebra operations. Resultantly, the computational time is reduced considerably, while the accuracy can be tuned by adjusting the truncation order of the Taylor expansion. DA has been applied widely in the field of orbital dynamics, e.g. asteroid encounter analysis (Armellin et al., 2010) and orbit conjunction analysis (Morselli et al., 2014). These dynamics-based methods are local and are difficult to efficiently handle dynamics with a large uncertainty set. They are also computationally intensive for high-order approximations of a high-fidelity system. For instance, DA fails when the high nonlinearity of dynamics, the large initial uncertainty set, and the long-term propagation prevent good convergence of the Taylor expansion, and a single Taylor expansion of the flow is usually not accurate enough to map the entire initial uncertainty domain. To overcome these problems, automatic domain splitting (ADS) was developed to automatically split the initial uncertainty domain into subdomains, over each of which a new Taylor expansion with good convergence is obtained (Wittig et al., 2015). ADS was firstly introduced by Wittig et al. (2015) and was applied to the orbital propagation of asteroid (99942) Apophis considering its initial state uncertainty. The non-impact and close-encounter regions of its state space with respect to Earth were identified and validated against point-wise simulations.

Extensive research has been performed on the dynamics and stability of orbital motion around small bodies with deterministic models (Scheeres, 2012). In general, when considering the irregular gravity of an asteroid, the retrograde orbit is found to be more stable than the prograde orbit. When considering the SRP perturbation, the most stable orbit is the so-called solar terminator orbit (STO), a specific type of polar orbits whose orbital plane precession rate is equal to the rate of the mean orbital motion of the small body around the Sun, i.e. its orbital plane always faces towards or away from the Sun perpendicularly. An STO is preferred when the SRP perturbation is strong. Most of these studies investigated the stability of the orbital motion with respect to the perturbation or uncertainty of the initial conditions of the spacecraft. However, there are limited studies addressing the effects of uncertainties of either the gravity or the SRP on the dynamics or robustness of motion around small bodies. Using the MC method and with the sample asteroid Stein, Melman et al. (2013) investigated the effects of its uncertain gravity on the evolution of the STO. The sensitivity of the STO to the gravity

uncertainty was found to become stronger if the gravity of the asteroid is weaker. For the small asteroid Bennu with a weak gravity field, a frozen-STO was found to be more robust against the execution uncertainties or errors than a circular-STO (Hesar et al., 2017), based on the averaged dynamics and the MC simulations. These studies focused on the effect of uncertainties on the STOs, without investigating the effects of uncertainties on the non-STOs. However, studying orbits with different geometries requires a large number of samples for the MC simulations. Applying the DA method, Feng et al. (2019) propagated the uncertainty of the irregular gravity field of asteroid Stein and investigated its effect on the orbits with different orbital geometry. Retrograde orbits were found to be more robust than prograde ones.

Very recent research demonstrates that 2016 HO_3 is a fast rotator and probably has a rather elongated shape (Li and Scheeres, 2021). However, this information is not included in this study for two reasons. Firstly, its shape and rotation are not well determined, so are the irregular gravity and its influence on the orbital motion. Secondly, the purpose of this study is to investigate the robustness of orbital motion to the uncertainty of the asteroid mass and the SRP. A more detailed approach would use a high-fidelity force model that includes perturbations such as those associated to the irregular gravity field, and then to carry out the robustness analysis to specific uncertain parameters such as the asteroid's mass or the SRP. However, since accurate information on the asteroid's non-spherical gravity is missing, its effect on the orbital motion is neglected in this preliminary study. Since the SRP is generally non-negligible, the effect of its uncertainty on orbital motion should also be studied. Considering the highly nonlinear dynamics and the large number of orbits with different geometries, this study extends previous research by applying the ADS to investigate the effect of uncertainties on both the asteroid's mass and the SRP on the general orbital motion around an extremely small body. The rest of this paper is organized as follows. Section 2 introduces the details of the ADS algorithm. Section 3 presents the dynamical model of orbital motion around 2016 HO_3 and evaluates the magnitudes of different perturbations. Section 4 applies the ADS algorithm to propagate the uncertainties and to investigate the sensitivity of orbital geometry to the uncertainties of both the central gravity and the SRP by evaluating their first split time, and resultantly identifying the robust region. The results are validated against numerical simulations. Section 5 concludes this study and gives prospects for future work.

2 The methodology of ADS

The DA method computes Taylor expansions of the flow of the dynamics up to arbitrary orders with automatic differentiation. The main idea of ADS is to determine the time at which the flow expansion over a given initial set is not capable of describing the dynamics with the required accuracy anymore. Once this situation is detected, the domain of the original polynomial expansion is divided along one of the expansion variables into two domains of the same size. Then, the dynamics is re-expanded around the new center points of the two domains, respectively, resulting in two separate polynomial expansions. Since the new expansions do not change the order, each of the new polynomials is identical to the original ones on its respective domain. This process is illustrated in Fig.1, in which the error is the truncation error measuring the difference between the n+1 time differentiable function and its Taylor expansion of order n, which is an absolute value. The parameter ε is the required accuracy. Following such a split procedure, the integration continues on each subdomain in the same manner until further splits are required or the final integration time is reached. The result is a list of Taylor expansions approximating the final state, each covering a subset of the domain of initial conditions.

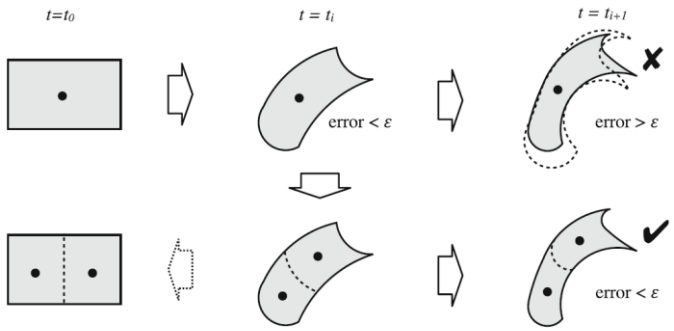

Figure 1 Illustration of the propagation process with ADS (Wittig et al., 2015).

In general, it is difficult to answer when exactly a polynomial needs to be split, and the direction of the split for the case of multivariate polynomials. To address this problem, the following method was implemented. For n-th order Taylor expansions, the size of the n + 1 order terms of the polynomial is estimated based on an exponential fit of the size of all the known non-zero coefficients up to order n. If the size of this truncated order becomes too large (e.g. larger than ε), the polynomial is split. Similarly, if the size of this truncation error for one specific variable is the largest or contributes the most to the total truncation error of the polynomial, then the split occurs in the direction of this variable. This approach maximizes the impact of the splitting procedure on the reduction of the approximation error.

During the splitting process, the split direction strongly depends on the parametrization of the initial conditions and can occur automatically along all variables that contribute to the truncation error. However, the initial condition can be parametrized such that the expansion splits mainly along a few or even just one of the directions, corresponding to the variables that the dynamics is more sensitive to. In addition, the number of the maximum split times and the minimum domain size can be predefined and modified, according to the requirements on the efficiency and accuracy. It is pointed out here that it is possible that some subdomain cannot be mapped to the end of the integration due to the limitation on the minimum domain size. Moreover, the earlier the splits occur and the more number of splits appear within a specific region, the stronger the nonlinearity of the dynamics is in this region, as strong nonlinearities are difficult to be managed with a single Taylor polynomial. For the DA-based numerical integration, the Dormand-Prince Runge-Kutta 7/8 integration scheme with the 7th order solution for step size control and the 8th order solution for propagation is used. The reader can refer to Wittig's paper (Wittig et al., 2015) for a more detailed description and demonstration about ADS.

3 Dynamical Modelling

The equation of motion for an object located at $\boldsymbol{r} = (x, y, z)$ in an asteroid-centered inertial reference frame is given as

$$\ddot{\boldsymbol{r}} = \boldsymbol{F}_{acc} = -\frac{\mu}{r^3}\boldsymbol{r} + \boldsymbol{F}_{SRP} + \boldsymbol{F}_{third\_body} \tag{1}$$

where the first term on the right-hand side of the equation is the acceleration from the central gravitational force and $\mu = Gm$ is the gravitational constant of the asteroid. The second and the third terms are the SRP perturbation and the third-body perturbation from the Sun and Earth, respectively. For the cannonball model of the s/c, $\boldsymbol{F}_{SRP}$ can be expressed as

$$\boldsymbol{F}_{SRP} = -(1+\eta)\cdot\rho_0\Delta_0^2\cdot\frac{S}{m}\cdot\left(\frac{\boldsymbol{\Delta}}{\Delta^3}\right) = -(1+\eta)\cdot\rho_0\cdot\frac{\Delta_0^2}{\Delta^2}\cdot\frac{S}{m}\cdot\left(\frac{\boldsymbol{\Delta}}{\Delta}\right) \tag{2}$$

in which η is the reflection coefficient of the s/c and $\eta = 1$ is for the ideal mirror reflection, $\frac{S}{m}$ is the area-to-mass ratio of the s/c, ρ_0 is the solar radiation flux at the reference distance Δ_0 (e.g. $\rho_0 = 4.56 \times 10^{-6}$ Pa at a distance of 1 AU). And $\boldsymbol{\Delta} = \boldsymbol{r}_\odot - \boldsymbol{r}$ is the relative position vector of the Sun to the s/c, as indicated in Fig.2. According to this cannonball model, the direction of the SRP perturbation

given in Eq.(2) is always parallel to the relative position vector of the Sun to the spacecraft. Therefore, the uncertainty is only considered on the magnitude of the SRP; i.e., the uncertainty on the SRP's direction is neglected.

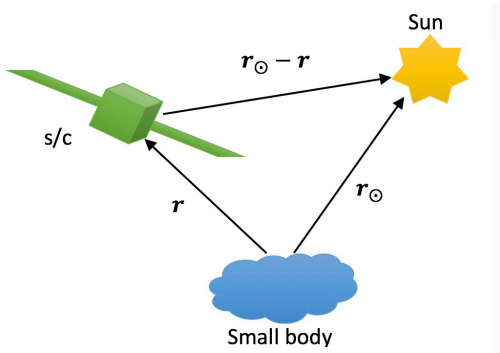

Figure 2 Illustration of the geometry of the s/c and Sun in the asteroid-centered inertial frame.

The third-body acceleration $\boldsymbol{F}_{third\_body}$ is given as

$$\boldsymbol{F}_{third\_body} = -GM\left(\frac{\boldsymbol{r}_{third}}{{r_{third}}^3} - \frac{\boldsymbol{\Delta}}{\Delta^3}\right) \tag{3}$$

in which GM is the gravitational constant of the third body.

For the convenience of the following numerical simulations, this dynamical system is normalized with the units of mass, length and time defined as

$$[M] = m_{HO3}, [L] = R_{HO3}, [T] = \sqrt{\frac{[L]^3}{G[M]}}$$

in which G m_{HO3} = 4.9781×10^{-11} km^3/s^2 and R_{HO3} = 44.7 m are the gravitational constant and reference radius of 2016 HO_3 (de la Fuente Marcos & de la Fuente Marcos, 2016), respectively. Accordingly, the value of the time unit is 1177 s. Therefore, the relationship between the normalized and the original accelerations can be obtained as

$$[a] = \frac{d^2 r}{d\tau^2} = \frac{d^2 \frac{R}{[L]}}{d\left(\frac{t}{[T]}\right)^2} = \frac{[T]^2}{[L]} \cdot \frac{d^2 R}{dt^2} = \frac{[T]^2}{[L]} \cdot a$$

Given the values of the area-to-mass ratio and reflection coefficient of the s/c to 0.02 m^2/kg and 0.4, respectively, the magnitudes of the forces on the s/c around 2016 HO_3 at different distances to 2016 HO_3 are obtained and given in Fig.3.

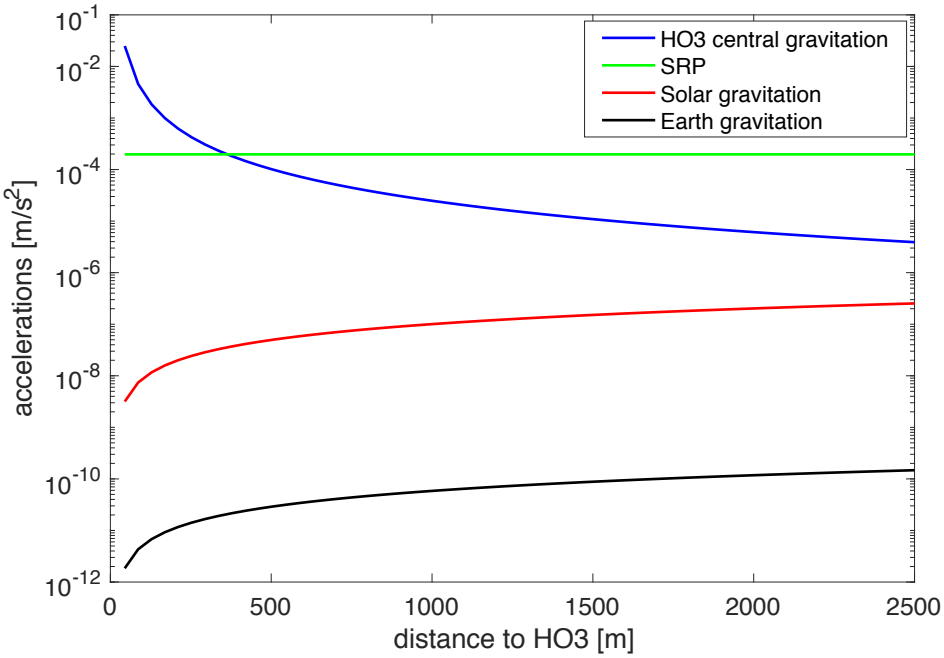

Figure 3 The magnitudes of the forces at different distances to 2016 HO_3.

It can be seen that the SRP is the dominant perturbation and becomes even larger than the central gravitation of 2016 HO_3 when the orbital altitude approximately exceeds ten times the reference radius of 2016 HO_3. The strength of the Sun's third-body perturbation is about 4 or 5 orders of magnitude smaller that of the SRP, and the Earth's third-body perturbation is even weaker and can be ignored. Therefore, the central gravitation, SRP and the Sun's third-body perturbation are the forces considered in the following simulations. Since the DA-based ADS method is used to obtain the high-order expansion of the state flow w.r.t. the uncertain parameters that are denoted as $\boldsymbol{p}$, the first step is to initialize $\boldsymbol{p}$ as a DA variable

$$[\boldsymbol{p}] = \boldsymbol{p} + \delta\boldsymbol{p}$$

where $\delta\boldsymbol{p}$ represents the deviation from the nominal value of $\boldsymbol{p}$. As discussed in the introduction, both the uncertainties of the central gravitation and the SRP are considered. Therefore, the uncertain parameter vector is specified as $\boldsymbol{p_0} = (\mu, F_{SRP})$ and $\boldsymbol{\delta p_0} = (\delta\mu, \delta F_{SRP})$, and the μ and F_{SRP} terms are expressed as DA variables as

$$\begin{cases} [\mu] = \mu + \delta\mu \\ [F_{SRP}] = F_{SRP} + \delta F_{SRP} \end{cases}$$

Since we do not consider the attitude of the s/c w.r.t. the Sun, we assume the direction of the SRP does not have uncertainty and we only consider the uncertainty of the magnitude of SRP in this study. Therefore, as a demonstration, the corresponding first-order expansion of the dynamics defined in Eq.(1) is given as

$$\ddot{\boldsymbol{r}} = \boldsymbol{F}_{acc} \approx \boldsymbol{F}_{acc}(\mu, F_{SRP}) + \boldsymbol{F}_{acc\_\mu} \cdot \delta\mu + \boldsymbol{F}_{acc\_SRP} \cdot \delta F_{SRP}$$

in which $\boldsymbol{F}_{acc}(\mu, F_{SRP})$ is the dynamics without uncertainties and $\boldsymbol{F}_{acc\_\mu}$ and $\boldsymbol{F}_{acc\_SRP}$ are the derivatives of the total acceleration force $\boldsymbol{F}_{acc}$ w.r.t. μ and F_{SRP}, respectively. The high-order expansions are obtained based on auto-differentiation.

4 Numerical Simulations

4.1 The uncertainties of central gravity μ and SRP

The heliocentric orbital elements of 2016 HO_3 are given in Table 1 and they are used in the following simulations. According to (Jin et al., 2019), the best estimation of the gravitational parameter of 2016

HO_3 is equal to 4.9781×10^{-11} $\pm1.1378\times10^{-12}$ km^3/s^2, with a 3σ error of 2.29% (1σ at 0.76%). Since the uncertainty of the SRP is related to the shape and materials of the s/c, the 1σ value of σ_{SRP} is difficult to be determined accurately and therefore two values are used in the simulations, i.e. 8×10^{-4} (corresponding to about 10% of the normalized SRP) and 8×10^{-5} (corresponding to about 1% of the normalized SRP).

Table 1 Heliocentric orbital elements of 2016 HO_3 at epoch 2459600.5 (2022-Jan-21.0) TDB[1]

Elements	Value	1σ Uncertainty	Elements	Value	1σ Uncertainty
a (AU)	1.001137344063433	3.0786×10^{-9}	Ω (deg)	66.0142959682462	1.5236×10^{-5}
e	0.1029843787386461	2.4307×10^{-7}	ω (deg)	305.6646720090911	2.2155×10^{-5}
i (deg)	7.788928644671124	1.6941×10^{-5}	M (deg)	107.172338605596	2.3044×10^{-5}

Before proceeding to the systematic simulations and the analysis of their results, let us point out that the relationship between the expansion order and computational time consumption for different precisions is investigated and given in Fig.4. The example orbit with a semi-major axis at 1.4 and all other orbital elements at zero is propagated for the time interval of 40 dimensionless units (one dimensionless time unit corresponding to 1177 s), considering the 1σ uncertainties of μ and the SRP at 0.76% and 1%, respectively. For the same precision, the 6th-order expansion requires more computational time than the higher orders, since the lower-order expansion requires more splits because of its lower accuracy. The 8th-order expansion needs slightly more computational time than the 10th-order expansion, except for a precision of 1×10^{-9}. This phenomenon is caused by the interaction among the expansion order, the number of splits and the time interval of the integration. For this research, the expansion order of 8 and the error tolerance or precision ϵ of 1×10^{-8} is a good balance of both efficiency (computational time) and precision, and therefore it has been selected to carry out the following simulations.

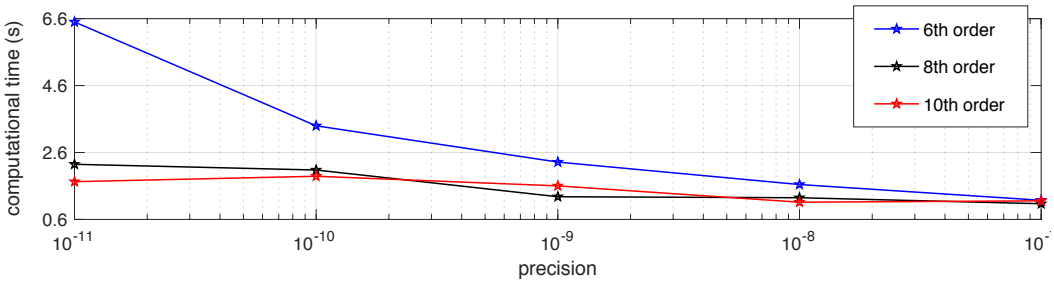

Figure 4 The relation between the precision and the computational time for different expansion orders.

4.2 Domain Split on the μ-SRP plane

In this section, by varying the semi-major axis and the propagation time of the orbital motion, the split of the initial uncertainty domain on the μ-SRP plane is investigated to identify the sensitivity of the dynamics on the uncertainties of μ and the SRP, respectively. Given the nominal values of μ and SRP, the motion will escape rapidly for a semi-major axis larger than 4.76 (one unit corresponding to 44.7 m), which is estimated by the formula $\sqrt{3\mu/16a_{SRP}}$ given in Scheeres (2012)[2]. Therefore, this paper focuses on the orbital motion with a semi-major axis a smaller than this value.

For the numerical simulations, values of a of 1.4, 2.5, and 3.5 (one unit corresponding to 44.7 m) have been selected. All the other orbital elements are set to zero. Specifically, the initial eccentricity is set

[1] https://ssd.jpl.nasa.gov/tools/sbdb_lookup.html#/?sstr=3752445

[2] Chapter 12, Page 263

to zero as the circular orbit is more preferable for mission operation. The initial inclination is set to zero as the prograde orbit is generally very unstable and is prone to split. The time interval of integration is firstly set to be five times the orbital period for each orbit, corresponding to the actual simulation times of 26, 62 and 103 (one unit corresponding to 1177 s), respectively. Their domain splits on the μ-SRP plane are given in Fig.5 and the numbers of splits are 1, 26 and 335, respectively. When the value of a increases from 1.4 to 3.5, more splits occur along the μ axis mainly due to the accumulation of the truncation error of the Taylor expansion with time. Along the SRP axis, the domain starts splitting for $a = 2.5$ and the splits number increases significantly for $a = 3.5$, because with the increase of the semi-major axis the SRP plays an increasingly significant role and the effect of central gravitation gradually recedes.

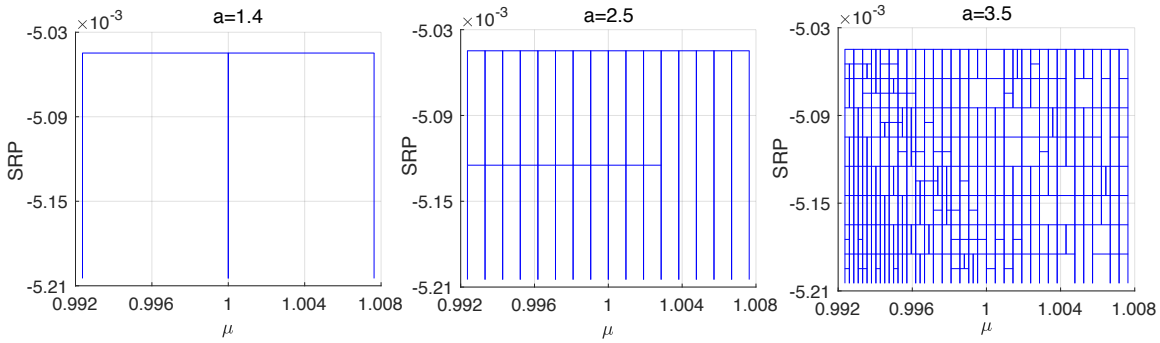

Figure 5 The domain split on the μ-SRP plane for $a = 1.4, 2.5, 3.5$ with the expansion order 8, the error tolerance 1×10^{-8}, and integration time of five orbital periods, i.e. t=5P for each of them. The units of semi-major axis *a* and time are 44.7 m and 1177 s, respectively.

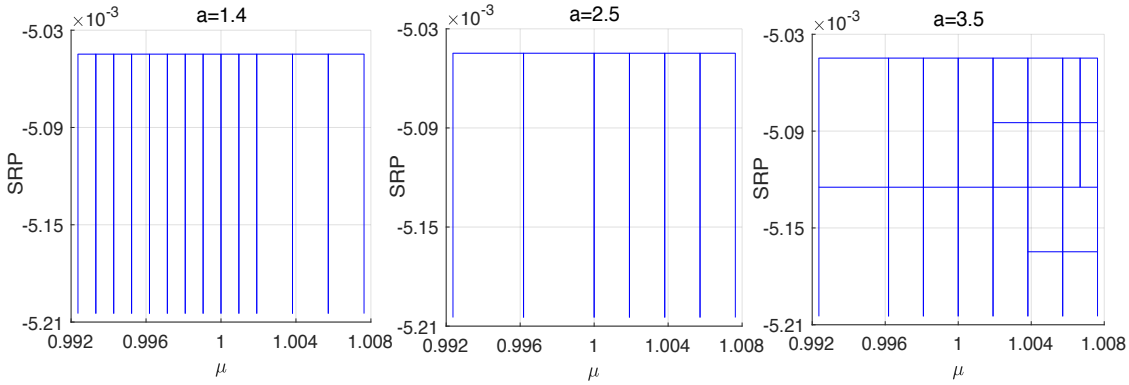

Figure 6 The domain split on the μ-SRP plane for $a = 1.4, 2.5, 3.5$ with the expansion order 8, the error tolerance 1×10^{-8}, and integration time t=55 for each of them. The units of semi-major axis *a* and time are 44.7 m and 1177 s, respectively.

For direct comparison, all the three orbits are integrated for the same time interval of 55 and their domain splits are given in Fig.6. It can be seen that the orbit with $a = 1.4$ has the most splits along the μ axis, indicating that the low-altitude motion is most sensitive to the uncertain central gravitation. For the orbit with $a = 3.5$, the splits along the μ axis are obviously less but a few splits start appearing along the SRP axis due to the larger influence of the SRP on the high-altitude orbit. The domain splitting of the middle-altitude orbit with $a = 2.5$ is the transition between those of the other two orbits. This phenomenon is in line with the fact that the low-altitude motion is dominated by the central gravitation and the high-altitude one is more influenced by the SRP perturbation. And the middle-altitude motion is kind of a balance between the dynamics of the central gravitation and that of the

SRP perturbation (Scheeres, 2012)[3]. In summary, the number of splits mainly depends on the nonlinear dynamics and the time interval of the integration, both of which are closely related to the accuracy of the Taylor expansion. It also demonstrates that ADS is an indicator of the strong nonlinearity of the dynamics and sensitivities to the uncertain variables, and its role in identifying the region of robust motion will be discussed in the following section.

4.3 Sensitivity analysis and regions of robust motion

For mission applications, two kinds of orbits are mainly considered. One is the regular circular orbits (RCO), an orbital motion that is viable only if the s/c is very close to 2016 HO_3. The other one is the STO mentioned in the introduction, which is obtained in the 2016 HO_3-centered co-rotating frame that coincides with the 2016 HO_3-centered inertial frame at the initial epoch in this study. Its initial condition is transformed back to the 2016 HO_3-centered inertial frame for the following numerical simulations.

4.3.1 Map of the first split time on the $a - i$ plane of RCO

To analyze the effects of the uncertain gravity field and SRP on orbits with different geometries, circular orbits with different combinations of a and i are simulated. For a circular orbit, given the inclination i, the ascending node Ω and $u = \omega + f$ fully describe the orientation of this circular orbit and the position of the initial point on it, respectively. Since we mainly consider the orbital geometry for the simulations in this section, orbital elements a and i are gridded within the range of $a \in [1, 4]$ (one unit corresponding to 44.7 m) and $i \in [0, 180°]$, respectively, u is set to zero and Ω is sampled every 45° from 0° to 180°. For each orbit, the time epoch when the first split occurs is recorded and is normalized by the orbital period of this two-body orbit. The corresponding map of the first split time is generated on the $a - i$ plane and is given in Fig.7, where all the plots A have the same value of SRP uncertainty at 8×10^{-5} and all the plots B have a larger value of 8×10^{-4}.

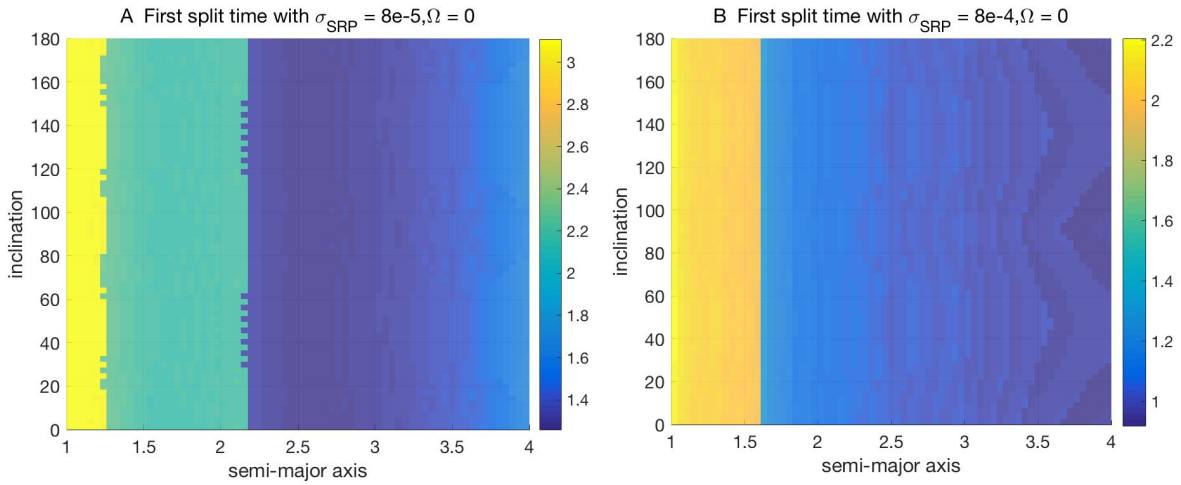

[3] Chapter 14, Page 296

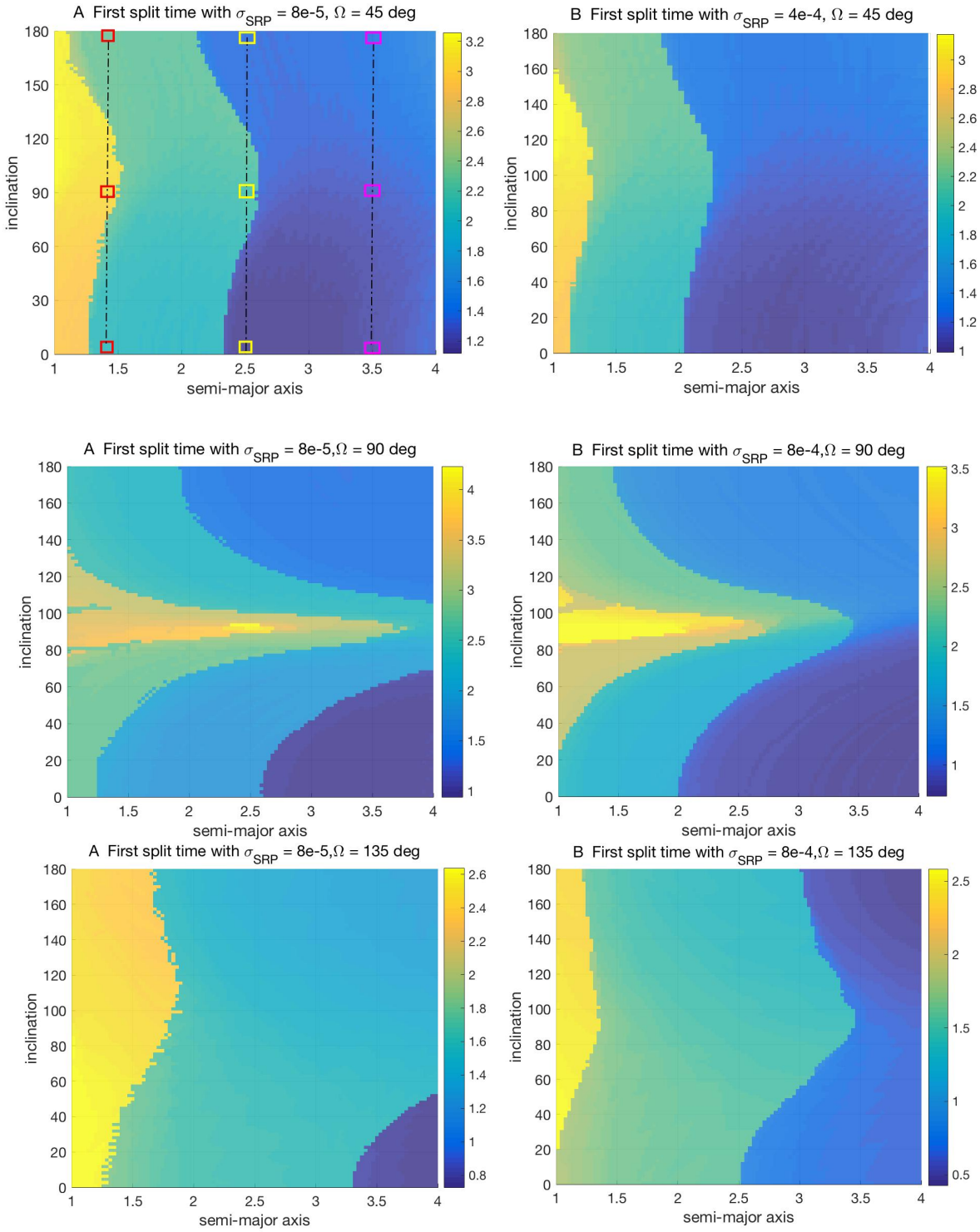
A First split time with σ_{SRP} = 8e-5, Ω = 45 deg
B First split time with σ_{SRP} = 4e-4, Ω = 45 deg
A First split time with σ_{SRP} = 8e-5,Ω = 90 deg
B First split time with σ_{SRP} = 8e-4,Ω = 90 deg
A First split time with σ_{SRP} = 8e-5,Ω = 135 deg
B First split time with σ_{SRP} = 8e-4,Ω = 135 deg
inclination
semi-major axis

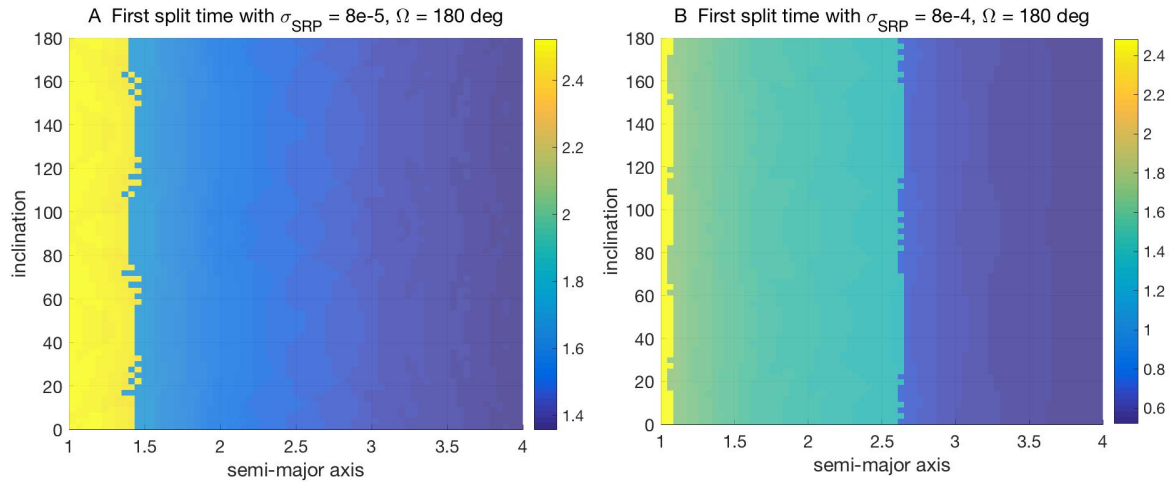

Figure 7 Map of the first split time on the $a - i$ plane for different values of σ_{SRP}. The units of *x* and *y* axes are 44.7 m and 1°, respectively. The color bar is the integration time normalized by its orbital period when the first split occurs.

For all the plots, the yellow region located closest to the asteroid that splits the latest is the most robust region in terms of orbital motion, due to the fact that the central gravitation of 2016 HO_3 dominates the dynamics in its vicinity and the SRP plays the role of a small perturbation. When moving further away from 2016 HO_3, the orbital motion becomes less robust as indicated by the light green or light blue region with a smaller value of the average first split time, where the central gravitation becomes weak and the SRP perturbation is stronger. Further away, there is a large blue area on the right with the smallest average first split time, where the robustness of the motion is reduced further due to the very strong SRP perturbation. It can be seen that the general structure of the plot A is similar to that of plot B for the same initial conditions. However, there are also obvious differences between plots A and plots B mainly on the location and size of the colored-regions. For plot B with a large value of the SRP uncertainty, the yellow region or the most robust region is only restricted to the extremely close distance to 2016 HO_3. This is due to the fact that, for the same accuracy requirement, larger uncertainty sets need the domain to be divided sooner because the radius of convergence in the SRP is fixed.

Specifically, for both $\Omega = 0°$ and 180°, the different colored-regions distribute vertically along the semi-major axis, indicating that orbits with the same inclination have similar robustness against the uncertainties and the robustness is only affected by the distance of the orbit to the body. For $\Omega = 45°$, 90° and 145°, it is obviously seen that most of the colored regions near the polar region have bulges in the right direction, especially for the low- and middle- altitude orbits and for the case of $\Omega = 90°$. This indicates that the polar orbit has the best robustness for non-zero and non-180° ascending node cases. In addition, for all the plots of $\Omega = 45°$, 90° and 145°, the lower half is orange colored and the upper half is yellow colored. The yellow color indicates later splitting times. In general, the lower half has deeper color than the upper half, which indicates an earlier split and demonstrates that the retrograde orbits generally split slightly later than the prograde ones and are more robust. Compared with the conclusion in Feng et al. (2019) that the retrograde orbits are generally much more stable than the prograde ones, this conclusion is weakened due to the consideration of a much stronger SRP perturbation w.r.t. the weak gravity of 2016 HO_3 (Scheeres, 2012)[4]. Finally, it is found that the first splitting time generally appears later for $\Omega = 90°$ among all the cases. Therefore, the polar orbit with 90° ascending node is the most robust, as will be investigated further in Section 4.3.3.

[4] Chapter 12, Page 272

4.3.2 *Numerical Integrations of the sample RCOs*

For a straightforward evaluation of stability of the orbit motion, nine sample orbits marked as squares are selected from plot A of $\Omega = 45°$ in Fig.7 for numerical integrations, i.e. orbits with $a = 1.4, 2.5, 3.5$ (one unit corresponding to 44.7 m) and $i = 0°, 90°, 180°$ for each value of a, respectively. Since a, e and i are the most relevant orbital elements and i is found to have very slight variations, only the evolutions of a and e are shown in Fig.8 for each orbit with the integration time of 3, 5 and 1.5 orbital periods, respectively. It is seen that for the three different values of a, all the polar orbits indicated by the red lines have the smallest variational amplitudes in semi-major axis and also the smallest increasing rate of eccentricity, compared with those of the equatorial orbits with $i = 0°$ and 180°. The black dash-dot lines in each evolutionary plot of e indicate the impact eccentricity for each specific value of a. The non-polar orbits always reach this line much earlier than the polar orbits. For the equatorial orbits with $a = 1.4, 2.5, 3.5$, they can complete approximately three, two and one orbital revolutions, respectively, before impacting on the small body, due to the perturbation of the SRP. Therefore, the polar orbits stay closer to its initial or original trajectory, which are very useful or applicable to real mission operations that prefers free orbital motion (without maneuvers) meeting accuracy requirements of observations for radio or laser tracking and navigation (Hussmann et al., 2012). In addition, it was also discovered in our previous study that the polar orbits are generally more stable. Orbital eccentricity of non-polar orbits, including the equatorial ones, can be excited to very large values which leads to impact with the asteroid (Feng and Hou, 2019). The results in Fig.8 also support this scenario.

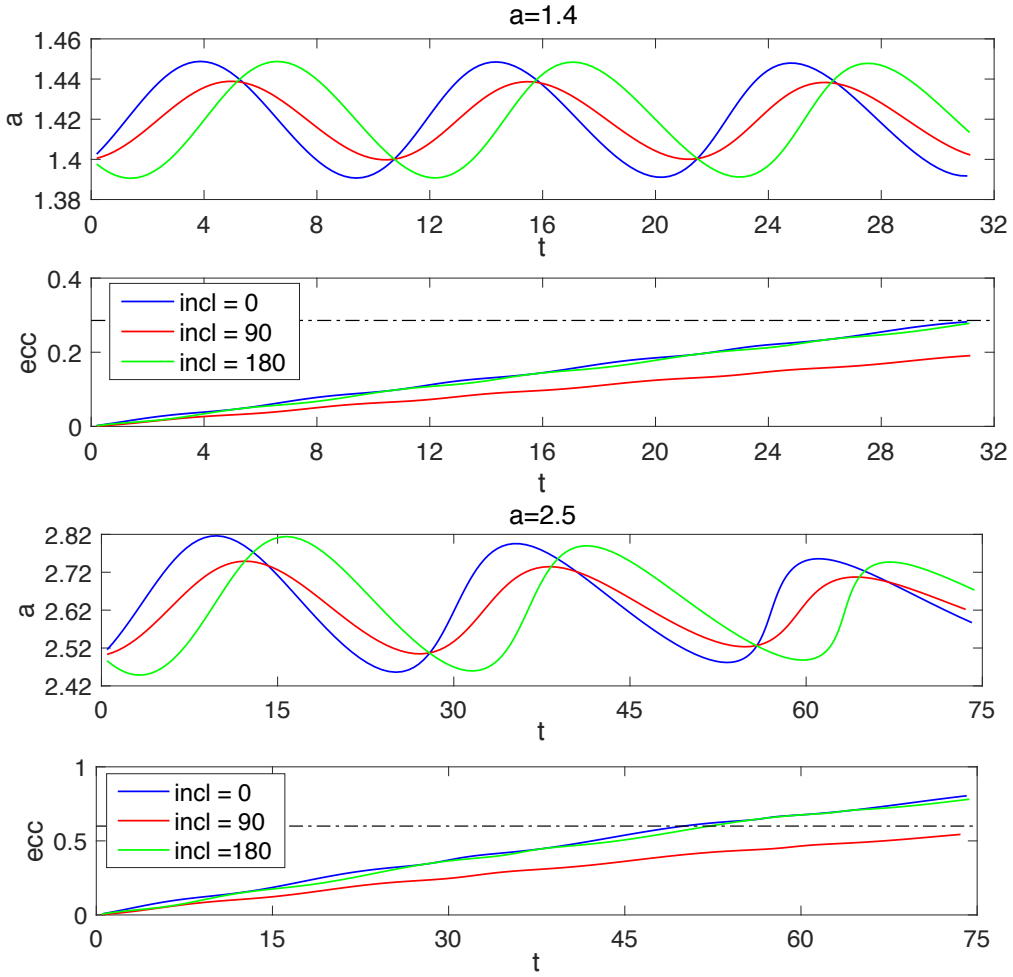

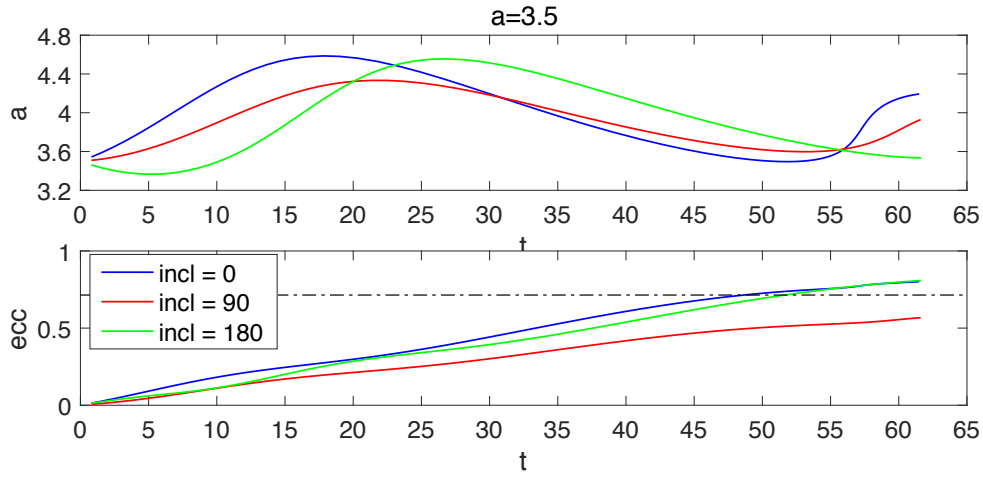

Figure 8 The evolutions of semi-major axis and eccentricity of the sample orbits from Fig.7A. The units of semi-major axis *a*, the inclination *i* and time *t* are 44.7 m, 1° and 1177 s.

4.3.3 Map of the first split time on the $a-\Omega$ plane of polar orbits and STO

Following the above investigations, this section explores the polar motion in more detail. For polar orbits, as the ascending node Ω determines the orientation of the orbit in space, a map of the first split time is generated on the $a-\Omega$ plane for the sensitivity analysis. The other orbital elements are set as $e=0, \omega=0°, i=90°$ with the same uncertainty values of the gravity and the SRP as in the previous section.

In Fig.9A, for $\Omega<90°$, the rectangular region consists of four colour regions transiting from the yellow one in the upper left corner to the deep blue one in the lower right corner, i.e. from the most to the least robust motion. For $\Omega>90°$, the structure of the map consists of three colour regions transiting from the yellow one in the lower left corner to the deep blue one in the upper right corner, i.e. from the most to the least robust motion. Since the first split time given in Fig.9A is the time normalized by the orbital period of the two-body orbit, we also give in Fig.9B the value of the first split time without normalization by the orbital period. It is seen that in general the orbit close to the body splits faster than that far away from the body due to influence of the gravity. However, this is obviously not a monotonous trend, e.g. for $\Omega<30°$ the region near *a*=2 (pink ellipse) splits later than that near *a*=2.3 (green ellipse), due to the perturbation of the SRP. For both Fig.9A and Fig.9B, at the same distance to the small body, the first split occurs very late if the orbit is closer to the region of $\Omega=90°$ as demonstrated by the black dash-dot line, mainly due to the fact that this orbital geometry is more stable to the SRP perturbation. However, the normalized first split time is generally larger if the orbit is closer to the smaller body as shown in Fig.9A. Since the normalization by the orbital period partially removes the effect of the distance or the gravity, the influence of the SRP perturbation on orbits with different geometries is more obvious in the plots. In particular, the orbit closer to the body is less influenced by the SRP and therefore has a late (normalized) split time, as indicated both in Fig.9A and Fig.7.

In addition, we also record the minimum distance to the asteroid before the first split occurs and the corresponding time epoch (also normalized by the orbital period) on the $a-\Omega$ plane as Fig.9C and 9D. For the same semi-major axis, Fig.9C shows that the minimum distance is generally the same for the low- and middle-altitude orbits and has a relatively larger value around $\Omega=0°$ and 90° for high-altitude orbits. The minimum distance generally increases for larger altitudes of the orbit. It is seen that the structure of Fig.9D is very similar to that of Fig.9A, which means that the first split is closely related to the close encounter with the asteroid. However, they are not exactly the same due to the influence of the SRP. In addition, by comparing Fig.9B with Fig.9C, it is observed that in general the split occurs earlier when the minimum distance is smaller. However, they still have different patterns,

again indicating that the splitting behavior is not affected only by the achieved distances. To further investigate the role of the SRP on the splitting, the magnitude of the SRP perturbation is decreased to half of its original value, by reducing the area-to-mass ratio from 0.02 to 0.01, and the corresponding first split time plot is generated (also normalized by the orbital period) as reported in Fig.9E. Due to the weaker SRP perturbation, for the same uncertainty set as that of Fig.9A, the results in Fig.9E show a later split for the same combination of a and Ω, e.g. the shrinking of the two blue regions. This indicates that the domain splits later if the SRP perturbation is smaller. Therefore, the split is closely related to the close encounters with the asteroid and is essentially triggered by the nonlinearity caused by both the gravity and the SRP perturbation.

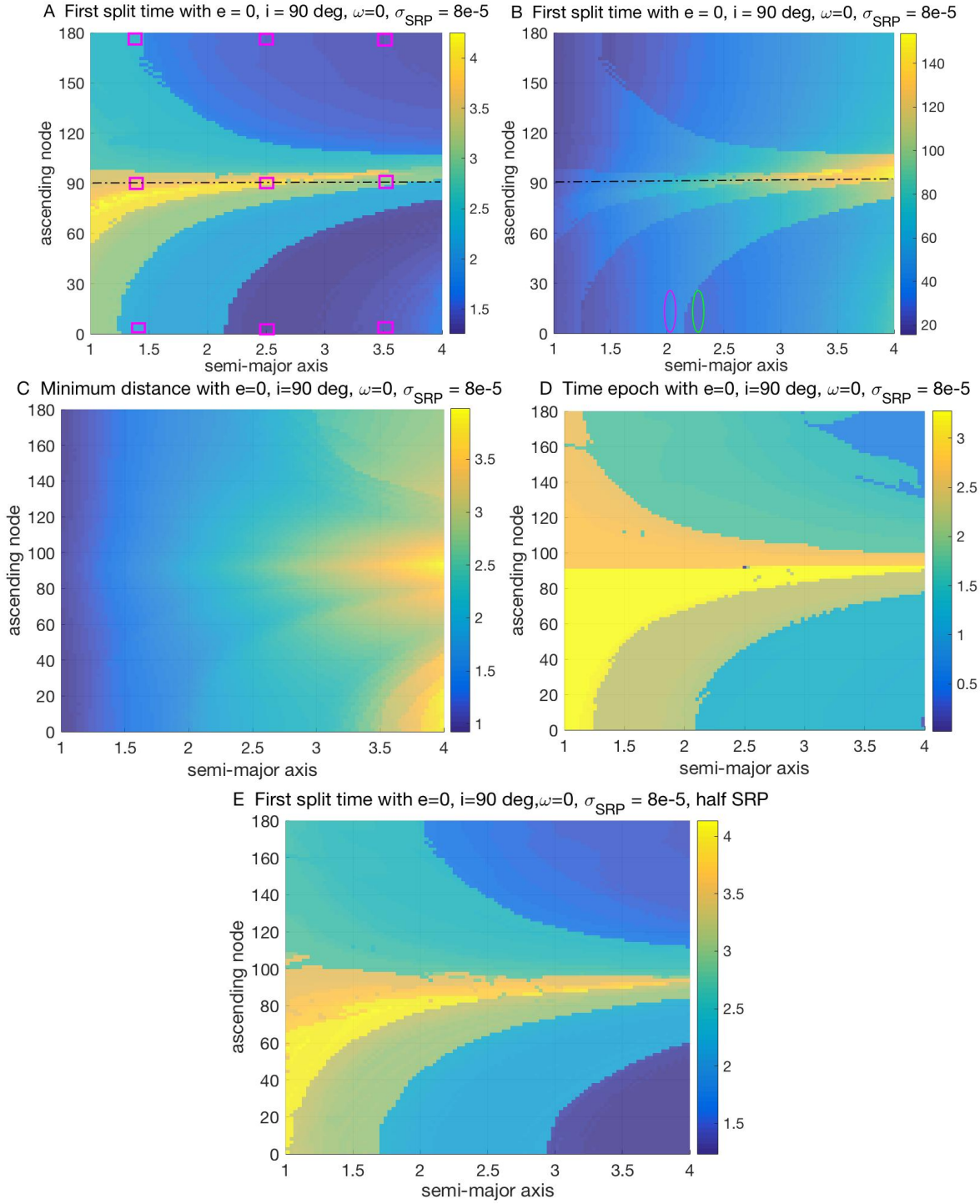

Figure 9 The first split time normalized by its orbital period on the $a - \Omega$ plane for different σ_{SRP}.

The color bar is the integration time normalized by its orbital period when the first split occurs. The units of *x* and *y* axes are 44.7 m and 1°, respectively.

The region in the vicinity of $\Omega = 90°$ corresponds to the terminator orbit, in particular the circular STO that has been extensively studied with the initial condition given as

$$e_0 = 0, i_0 = 90°, \Omega_0 = 90°$$

In addition, there is another type of terminator orbit called the frozen STO with its eccentricity and pericenter staying frozen, i.e. $\dot{e} = \dot{\omega} = 0$. Its initial condition is given as (Scheeres, 2012)[5]

$$e_0 = cos\Lambda, i_0 = 90°, \Omega_0 = \pm 90°, \omega_0 = \mp 90°$$

in which

$$tan\Lambda = \frac{3}{2}(1+\eta)\cdot\rho_0\Delta_0^2\cdot\frac{s}{m}\cdot\sqrt{\frac{a}{\mu\mu_s A(1-E^2)}}$$

where $\rho_0\Delta_0^2$ is explained in Eq.(2), a is the semi-major axis of the STO, *A* and *E* are the semi-major axis and eccentricity of the asteroid around the Sun. Due to the weak gravity of 2016 HO_3, the frozen eccentricity *e* as a function of a is very small as shown in Fig.10. Therefore, the frozen STO is a near-circular orbit for the scenario of 2016 HO_3.

As before, we select several sample polar orbits from Fig.9A marked with rectangular to simulate their orbital evolution for $a = 1.4, 2.5, 3.5$ (one unit corresponding to 44.7 m) and $\Omega = 0°, 90°, 180°$. The other orbital elements *e* and *i* are fixed to zero and 90°, respectively. Given $\Omega = 90°$, ω is set to 0° and -90° for the initial conditions of the circular and frozen STO, respectively. For other values of Ω, ω is fixed to 0° for a generalized polar orbit.

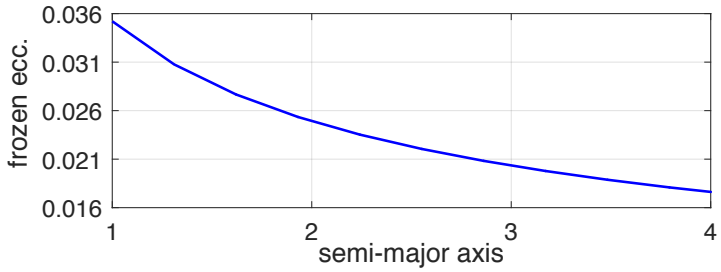

Figure 10 The eccentricity of a frozen STO at different semi-major axis. The unit of *x* axis is 44.7 m.

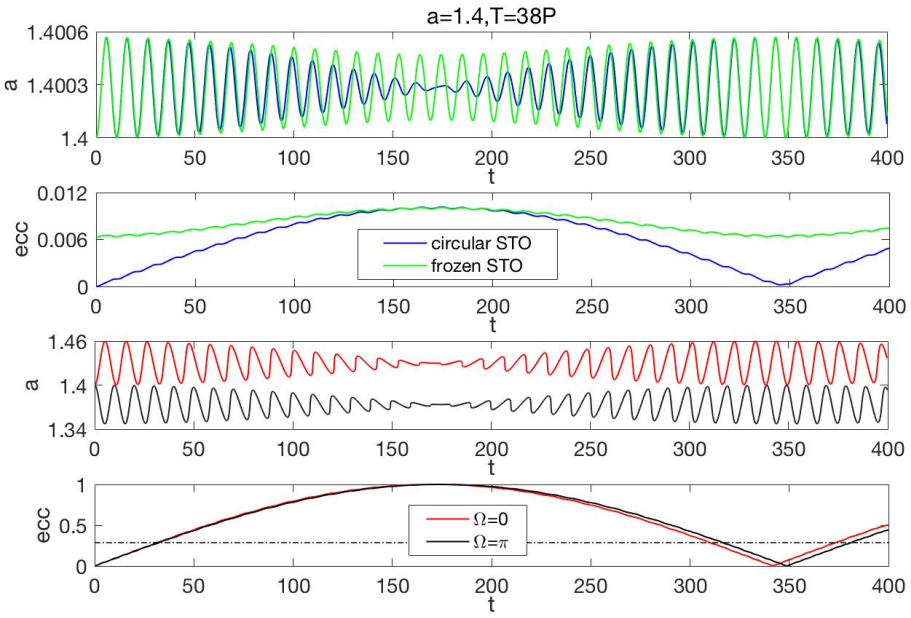

[5] Chapter 13, Page 282

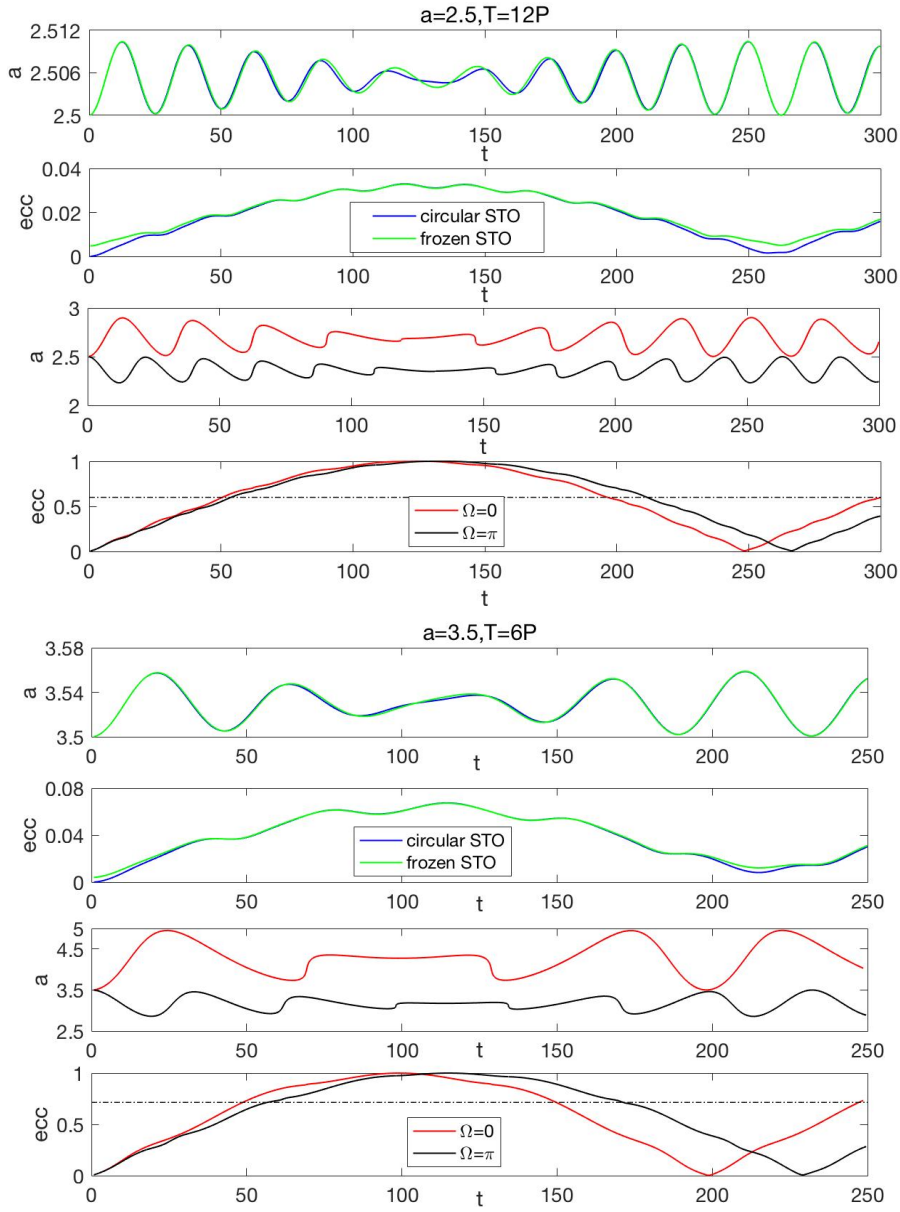

Figure 11 The evolutions of orbital elements a and e of the sample orbits from Fig.9. The units of semi-major axis a and time t are 44.7 m and 1177 s, respectively. Ω is in radian.

The evolutions of orbital elements a and e are given in Fig.11. The duration of the simulations is different for $a = 1.4, 2.5, 3.5$, respectively, to cover at least one revolution of each orbit. For all the sample orbits with $\Omega_0 = 90°$, i.e. the circular STO and frozen STO, they all have the smallest variations of both a and e, as indicated by the blue and green lines in the plots, respectively. Nevertheless, these orbits have long-term stability and stay well bounded, in terms of not impacting 2016 HO_3 and their distances to 2016 HO_3 not varying significantly. They are ideal candidates for orbits of mission operations. For sample orbits either with $\Omega_0 = 0$ (red lines) or 180° (black lines), their a and e have very large oscillations and after a short period of time their e reaches the impact eccentricity marked by the black dash-dot line, indicating their strong instability. Moreover, the analysis of these simulations is consistent with the first split time obtained in Fig.9, which proves that the first split map of ADS is an efficient tool to measure the nonlinear dynamics that is closely related to the stability of the motion.

For illustration, the sample orbits with $a = 2.5$ in three-dimensional inertial space are given in Fig.12 for the time interval of integration of 10P. It is seen that both the circular STO and frozen STO with $\Omega_0 = 90°$ are well bounded within a relatively small region, whereas the other two orbits spread

extensively in their original orbital plane and deviate far from the original orbits. Therefore, the STOs are recommended as robust orbits.

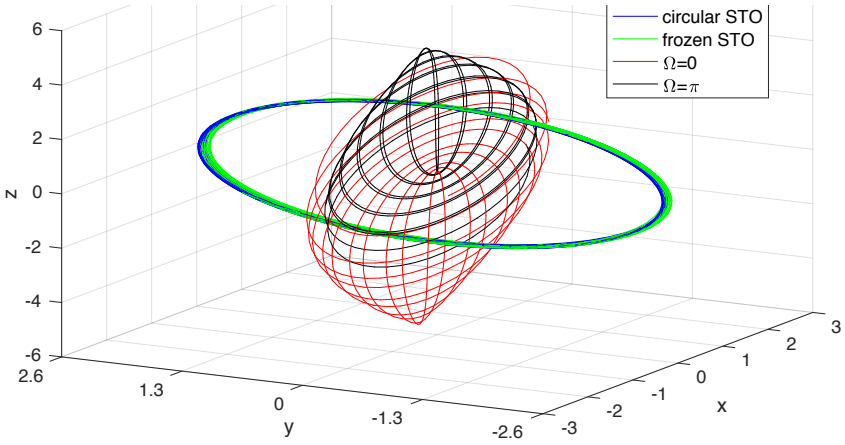

Figure 12 The orbit integration of sample orbits with $a = 2.5$ for the time interval of 10 orbital periods in the asteroid-centered inertia frame. The unit of *a*, *x, y, z* is 44.7 m. Ω is in radian.

4.4 Split history and bounds of the trajectory

This section focuses on obtaining and analyzing the split history and the bounds of the trajectory along their orbital evolution, due to the uncertainties of μ and SRP. Large and small SRP uncertainties are used, corresponding respectively to 10% and 1% of the SRP, respectively. Since 10% is a bit too large for a real scenario, we select the small case 1% with the uncertainty value 8×10^{-5} for the simulations in this section.

4.4.1 Split history of example polar orbits

Taking the example orbits with $a = 2.5$ (one unit corresponding to 44.7 m), $i = 90°$, $e = 0$, $\omega = 0°$ and for $\Omega_0 = 0°$ and $\Omega_0 = 90°$, respectively, the evolutions of a and e of both the reference trajectories (no split occurs) and the split trajectories are given in Fig.13. For orbits with $\Omega_0 = 0°$, we propagate till *t*=60 (one unit corresponding to 1177 s) that is the time after which many splits occur. It is seen that the first split occurs at about *t*=31.5. For orbits with $\Omega_0 = 90°$, it is propagated till *t*=200 and its first split occurs at about *t*=98 followed by two more splits at t=173 and t=180 as indicated by the blue and black lines. From the comparison of the first split time of these two orbits, it is proven that the terminator orbit is more robust to the uncertainties. In addition, comparing with the evolutions of a and e for $a = 2.5$ in Fig.11, it is seen that the split trajectories stay close to and follow the tendency of the reference trajectory.

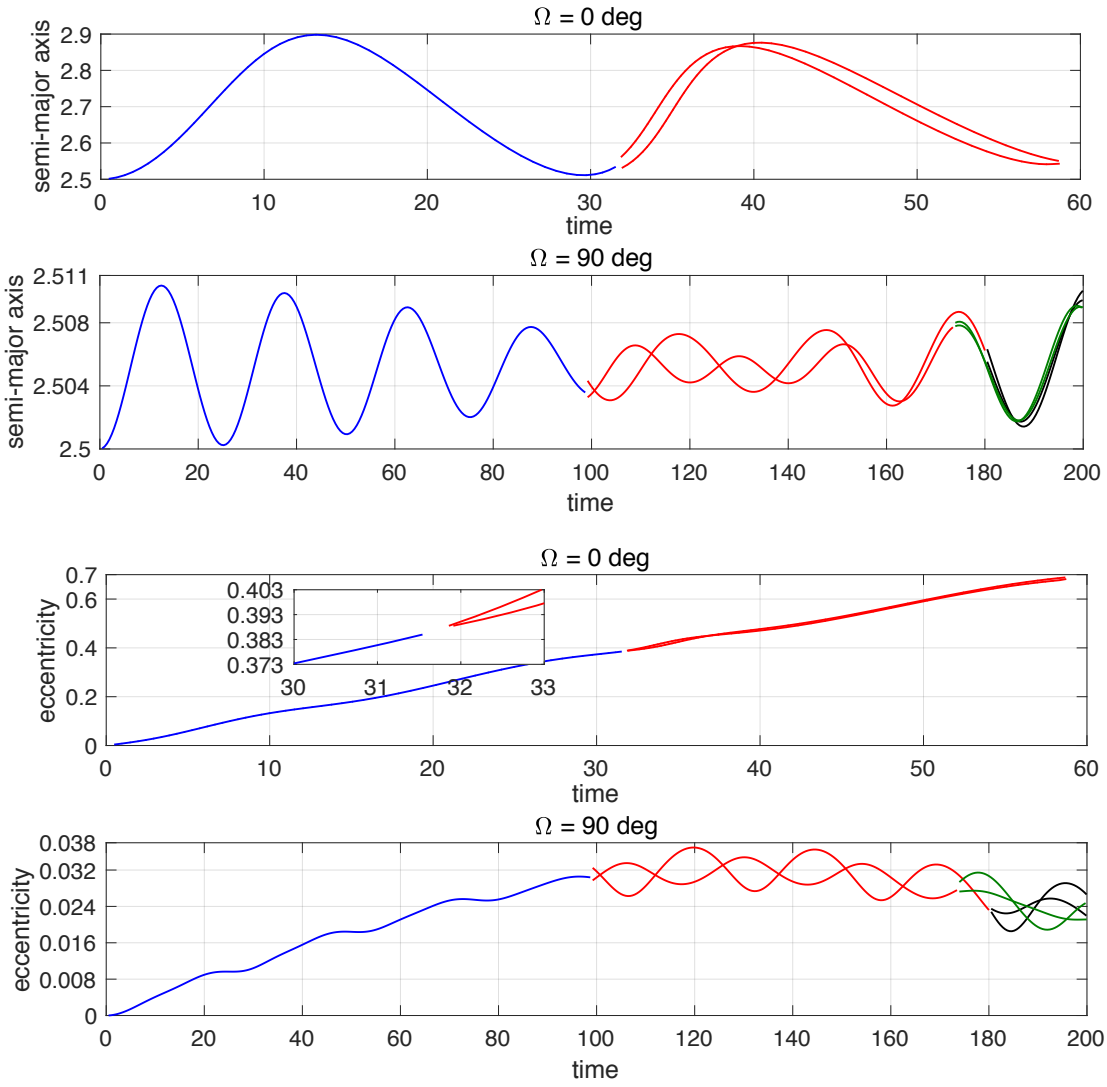

Figure 13 The split history of a and e for orbits with $a = 2.5$, and $\Omega_0 = 0°$ and $\Omega_0 = 90°$. The units of semi-major axis a and time are 44.7 m and 1177 s, respectively.

4.4.2 The bounds of the sample orbits

This section investigates the robustness of the polar motion by studying the bounds of the spacecraft distance to the asteroid, due to the uncertainties of both gravity and the SRP. The distance of the reference trajectory to the asteroid is named as reference distance. The uncertainty values of gravity and the SRP are 2.29% (3σ) and 8×10^{-5} (1σ), respectively. The following simulations are performed for all the example orbits from both Fig.7 and Fig.9. Once the high-order Taylor expansion w.r.t. the initial uncertainties is obtained, the outer bound of the range of the expansion at different times is then estimated by applying interval arithmetic (Moore et al., 2009). Therefore, the bounds are computed through the Taylor expansion of ADS. To validate the results, an MC simulation is performed. For each example orbit, it is propagated for 100 scenarios with different values of gravity and the SRP for each run. For the results shown in Fig.14, the red and black lines represent the reference distances and the MC simulations, respectively. The green and pink ones represent the upper and lower bounds estimated from ADS. For all the example orbits, the time intervals of their integrations are different and are truncated at different time epochs according to the divergence of the uncertainty propagation.

For all the sample orbits from Fig.7 with Ω_0=90°, the results are presented in Fig.14. It can be seen that polar orbits are the most robust and stable due to their narrow bounds and the smallest-

amplitude variations of the evolution of the distance. For example, for *a*=1.4 (one unit corresponding to 44.7 m), the resulting bounds of the distance due to the uncertainties at *t*=50 (one unit corresponding to 1177 s) are 0.619 for *i*=0° and 0.245 for *i*=180°, respectively. For *i*=90°, the bound is 0.186 at *t*=80, which is far smaller than the other two cases. The range of the distance varies between about 0.8 and 2 for non-polar cases and between 1.3 and 1.5 for the polar case, which is much narrower. In addition, for *a*=1.4, 2.5, 3.5, the closest encounter is at about *t*=42, 48 and 43 for zero inclination orbits and at about *t*=47, 62 and 60 for 180° inclination orbits. This indicates that the closest encounter with the asteroid always happen earlier for the orbit with 0° inclinations than the orbit with 180° inclinations, which is consistent with the map of the first split time of Fig.7.

For all the sample orbits from Fig.9 with i_0=90°, the results are presented in Fig.15. For the orbit with $a = 1.4$ and $\Omega_0 = 0°$, it is seen that its distance to 2016 HO_3 varies significantly and the range of the distance increases rapidly along with time by reaching between 0.9 and 1.95 at the truncated time *t*=40. The bounds are narrow at the beginning and extend evidently along with time. For the orbit with $a = 1.4$ and $\Omega_0 = 90°$, i.e. the STO, its distance to 2016 HO_3 varies slightly and is restricted between 1.375 and 1.425 until the end of the integration time *t*=100, which is much smaller than that of the polar orbit with $a = 1.4$ in Fig.14. In addition, the boundary of STO expands little along with the time, which also indicates its increased robustness. Similar phenomena are evident for orbits with $a = 2.5$ and $a = 3.5$, demonstrating that the STO indeed is more robust against environment uncertainties than other types of orbits. Since the distance of STO to the body is well restricted within small ranges, it is a good candidate for mission design.

For both Fig.14 and Fig.15, it is seen that the range of the distance enlarges significantly with the increase of a, due to the stronger SRP on high-altitude orbits. This conclusion agrees with the simulations in Section 4.3. Moreover, the bounds estimations of all the example orbits using ADS generally are in good agreement with these of the MC simulations until obvious overestimation occurs when the single Taylor expansion is not accurate enough over the whole uncertainty domain and the split of the domain is needed. From Fig.14, it can also be seen that the overestimation occurs especially when the motion is in close encounter with the asteroid, e.g. the lower bound (pink line) at about *t*=62 and 72 for $a = 1.4$, $i_0 = 90°$ and $\Omega_0 = 45°$, again indicating the nonlinearity fundamentally caused by the $1/r^2$ gravity. Improved bounds based on the Taylor expansions of these split trajectories can be well estimated, which is not displayed here as the main purpose of the current study is the sensitivity analysis. Nevertheless, in spite of the overestimation, the size and the evolution tendency of the uncertainty domain are well estimated. The obtained evolution of bounds provides a quantitative information to select trajectories that have the required robustness to uncertainties.

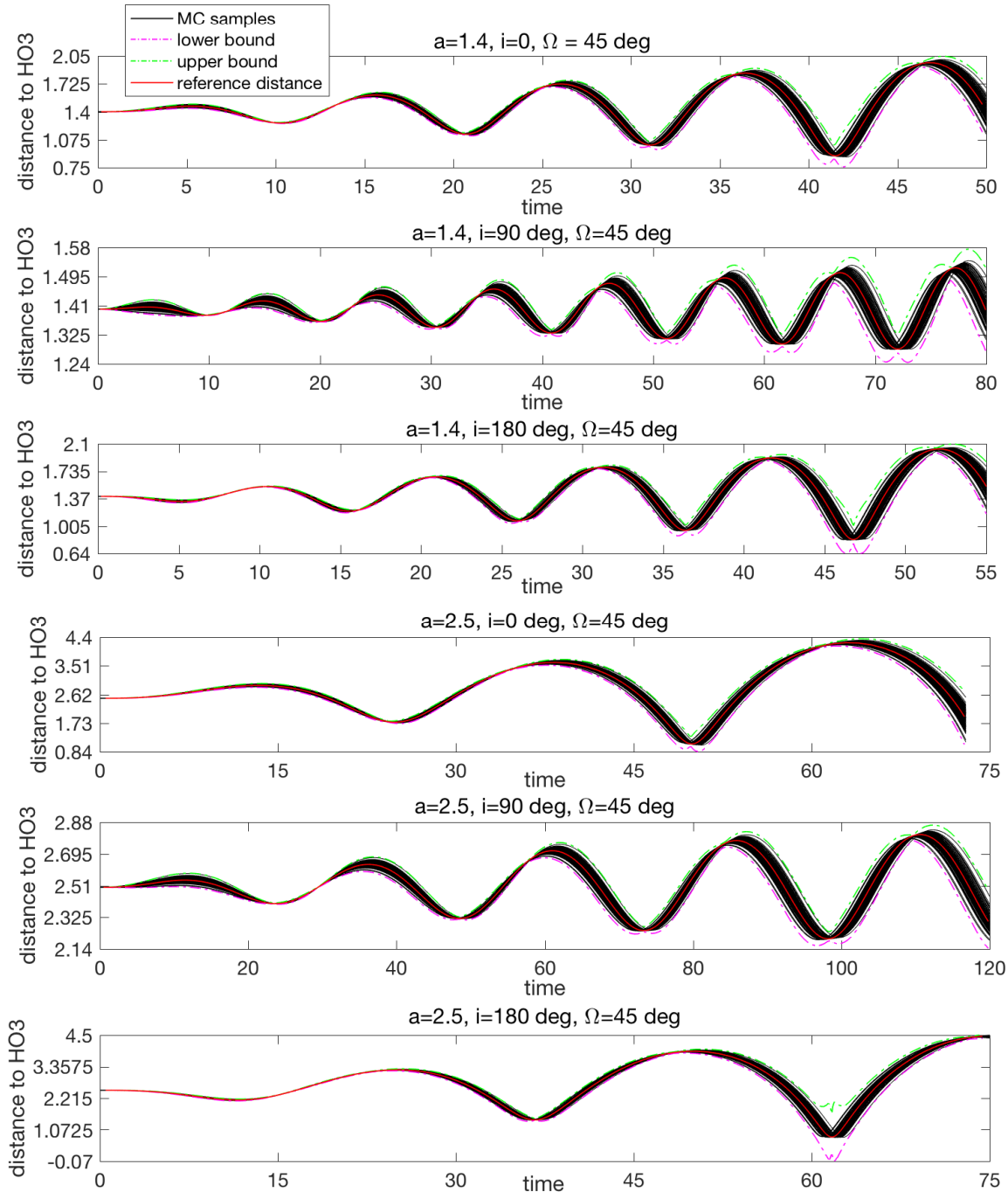
MC samples
lower bound
upper bound
reference distance
a=1.4, i=0, Ω = 45 deg
a=1.4, i=90 deg, Ω=45 deg
a=1.4, i=180 deg, Ω=45 deg
a=2.5, i=0 deg, Ω=45 deg
a=2.5, i=90 deg, Ω=45 deg
a=2.5, i=180 deg, Ω=45 deg
distance to HO3
time

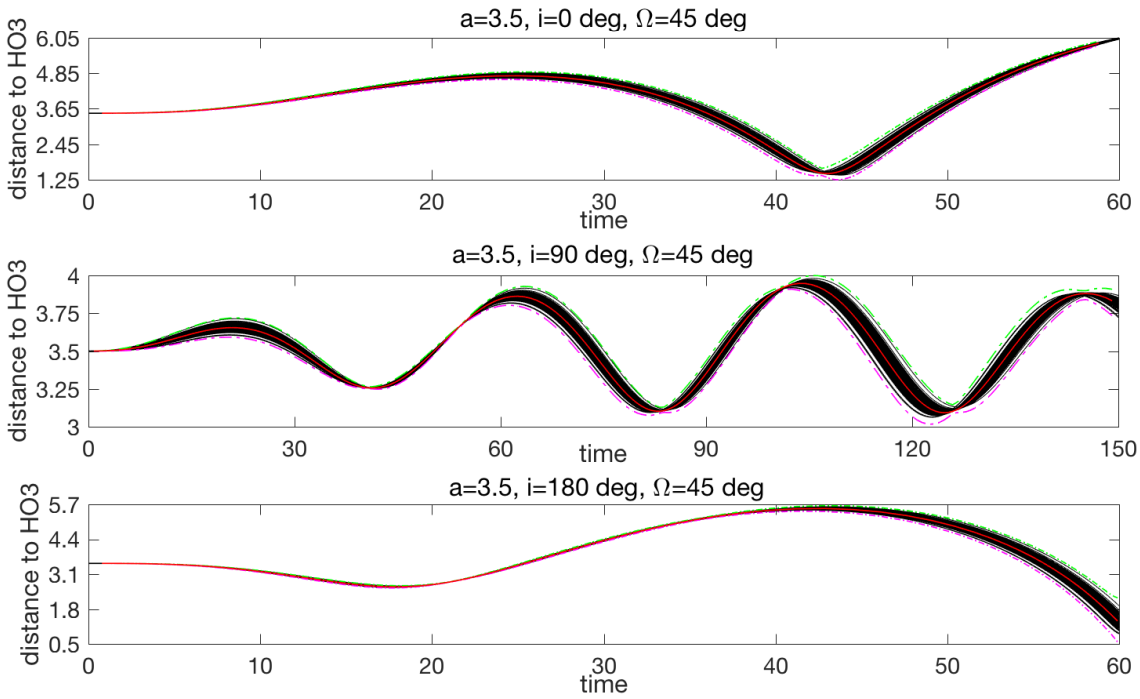

Figure 14 The distance to 2016 HO_3 of the reference trajectory (red solid line), the MC simulations (black solid lines) and the estimated bounds using ADS (green and pink dash lines) for the sample orbits from Fig.7. The units of semi-major axis *a* and time are 44.7 m and 1177 s, respectively.

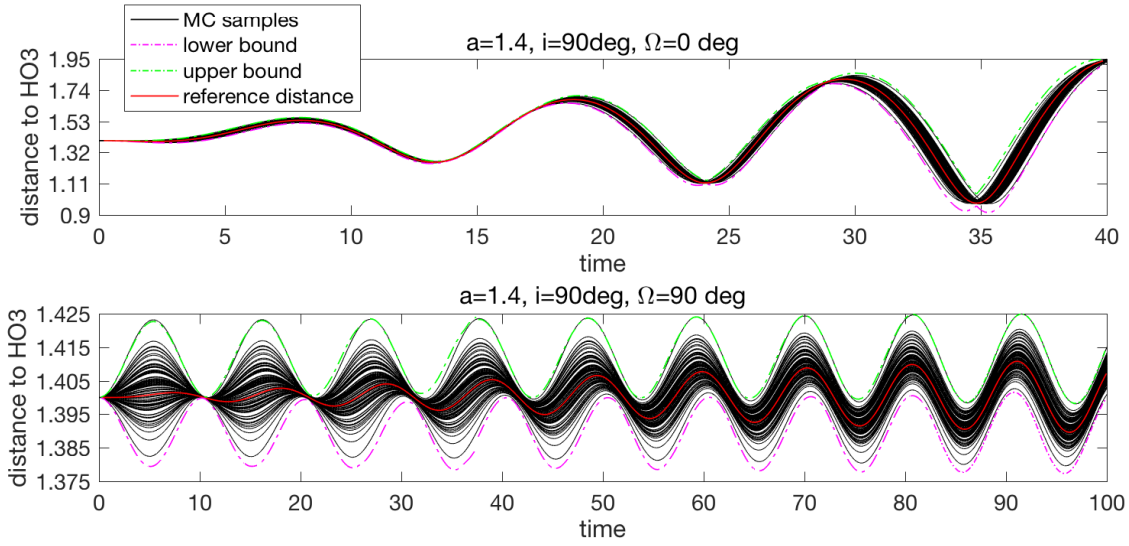

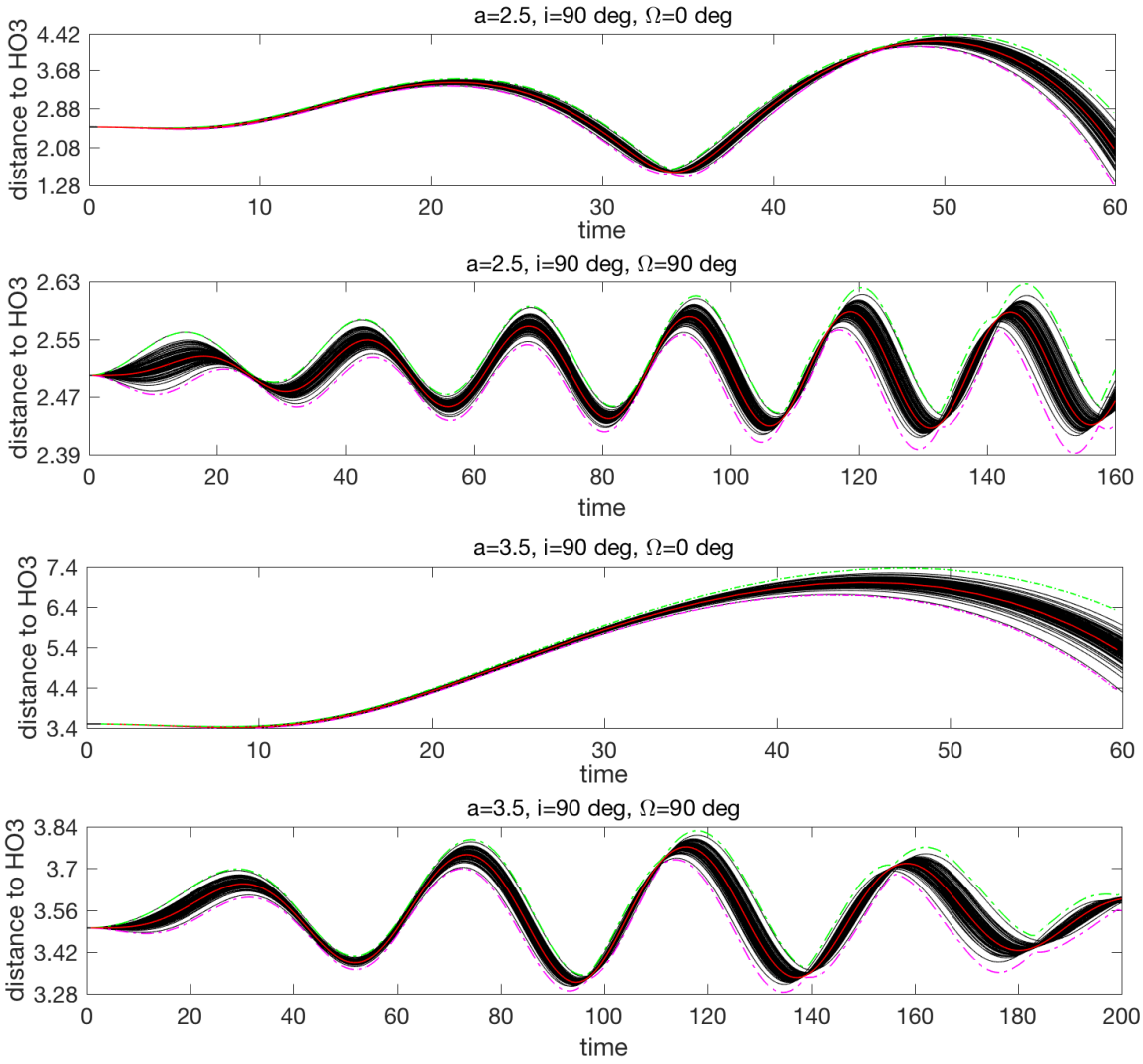

Figure 15 The distance to 2016 HO_3 of the reference trajectory (red solid line), the MC simulations (black solid lines) and the estimated bounds using ADS (green and pink dash lines) for the sample orbits from Fig.9. The units of semi-major axis *a* and time are 44.7 m and 1177 s, respectively.

5 Conclusions

By applying the ADS algorithm, the uncertainties of the asteroid's mass and the SRP are propagated along the orbital motion and their effects on orbits with different geometries are characterized, for the application to 2016 HO_3. The map of the first split time indicates the dynamical structure of the system in terms of nonlinearity and robustness. STOs are found to be more robust to the model uncertainties, making them good candidates for real mission orbits. These investigations prove that robust orbits do exist for very small bodies with very weak gravity. Moreover, the split history and bounds of the trajectory are evaluated for the sample orbits, and ADS is demonstrated to be an efficient tool to estimate the bounds of the motion. The evolution of bounds provides quantitative information for selecting the most attractive mission operative orbits.

In summary, this work contributes to systematically identifying the robust regions of orbital motion near a very small asteroid considering uncertainties in the force model and to efficiently estimating the bounds of the motion. For future work, the effect of the uncertainty on the initial state and on maneuvers executions will be investigated, as well as the effects of the irregular gravity field and the rotation rate of the small body.

Acknowledgement
This work is supported by Natural Science Foundation of China for Young Scientist with No. 11703013. X. Hou wishes to thank the support from the Natural Science Foundation of China with No. 11773017.

References

R. Armellin, P. Di Lizia, F. Bernelli-Zazzera, M. Berz, Asteroid close encounters characterization using differential algebra: the case of Apophis, Celestial Mechanics and Dynamical Astronomy, 2010, 107(4): 451-470.

A. Morselli, R. Armellin, P. Di Lizia, F. Bernelli-Zazzera, A high order method for orbital conjunctions analysis: sensitivity to initial uncertainties, Advances in Space Research, 2014, 53(3): 490–508.

V. Arnold, Mathematical Methods of Classical Mechanics. Springer, 2nd edition, 1989.

M. Berz, Modern Map Methods in Particle Beam Physics, Academic Press, New York, 1999: 82–96.

A. Cheng, A. Rivkin, P. Michel, et al., DART asteroid deflection test: Planetary defense and science objectives, Planetary and Space Science, 2018, 157: 104-115.

F. Dora, R. Vishnun, W. Richard, et al., Photometry and Spectroscopy of (469129) 2016 HO_3, AAS/Division for Planetary Sciences Meeting Abstracts, 2018, 50: 505.04.

J. Feng, R. Armellin, X. Hou, Orbit propagation in irregular and uncertain gravity field using differential algebra, Acta Astronautica, 2019, 161: 338-347.

J. Feng, X. Hou, Secular dynamics around small bodies with solar radiation pressure, Commun Nonlinear Sci Numer Simulat, 2019, 76: 71–91.

C. de la Fuente Marcos, R. de la Fuente Marcos, Asteroid (469219) 2016 HO_3, the smallest and closest Earth quasi-satellite, Monthly Notices of the Royal Astronomical Society, 2016, 462(4): 3441-3456.

S. Gur'yanov, T. Galushina, Study of the Dynamics of the Asteroid Kamo`Oalewa, Russian Physics Journal, 2021, 63(11): 1989-1996.

S. Hesar, D. Scheeres, J. Mcmahon, Sensitivity analysis of the OSIRIS-REx terminator orbits to maneuver errors, Journal of Guidance, Control and Dynamics, 2017, 40: 1–15.

H. Hussmann, J. Oberst, K. Wickhusen, et. al, Stability and evolution of orbits around the binary asteroid 175706 (1996 FG3): Implications for the MarcoPolo-R mission, Planetary and Space Science, 2012, 70(1): 102-113.

W. Jin, F. Li, J. Yan, et al., Simulation of global GM estimate of Asteroid (469219) 2016 HO_3 for China's future asteroid mission, EPSC-DPS Joint Meeting, 2019, 13: 15-20.

S. Julier, J. Uhlmann, H. Durrant-Whyte, A new approach for filtering nonlinear systems, in: Proceedings of IEEE American Control Conference, 1995, 1628–1632.

D. Lauretta, S. Balram-Knutson, E. Beshore, et al., OSIRIS-REx: Sample Return from Asteroid (101955) Bennu, Space Sci Rev, 2017, 212: 925–984.

X. Liu, D. Scheeres, The shape and surface environment of 2016 HO_3, Icarus, 2021, 357, 114249.

S. Maybeck, Stochastic Models, Estimation and Control, Academic press, New York, 1982.

J. Melman, E. Mooij, R. Noomen, State propagation in an uncertain asteroid gravity field, Acta Astronautica, 2013, 91: 8–19.

R. Moore, R. Kearfott, M. Cloud, Introduction to Interval Analysis. Cambridge University Press, 2009.

A. Pellacani, M. Graziano, M. Fittock, et al., HERA vision based GNC and autonomy, 8th European Conference for Aeronautics and Space Sciences (EUCASS), 2019.

D. Scheeres, Orbital Motion in Strongly Perturbed Environments: Applications to Asteroid, Comet and Planetary Satellite Orbiters. Springer-Praxis, London (UK), 2012.

D. Scheeres, J. McMahon, B. Bierhaus, et al., Janus: A NASA SIMPLEx mission to explore two NEO Binary Asteroids, AGU Fall Meeting Abstracts, 2020.

G. Terejanu, P. Singla, T. Singh, P.D. Scott, Uncertainty propagation for nonlinear dynamic systems using gaussian mixture models, Journal of Guidance, Control and Dynamics, 2008, 31(6): 1623–1633.

M. Vasile, C. Absil, A. Riccardi, Set propagation in dynamical systems with generalised polynomial algebra and its computational complexity, Commun Nonlinear Sci Numer Simulat, 2019, 75: 22–49.

S. Watanabe, Y. Tsuda, M. Yoshikawa, et al., Hayabusa2 Mission Overview, Space Sci Rev, 2017, 208: 3–16.

N. Wiener, The homogeneous chaos, Am. J. Math. 1938, 60(4): 897–936.

A. Wittig, P. Di Lizia, F. Bernelli-Zazzera, et al., Propagation of large uncertainty sets in orbital dynamics by automatic domain splitting, Celestial Mechanics and Dynamical Astronomy, 2015, 122(3): 239-261.

X. Zhang, J. Huang, T. Wang, Z. Huo, ZhengHe – A Mission to a Near-Earth Asteroid and a Main Belt Comet (PDF). 50th Lunar and Planetary Science Conference, March, 2019.